MDPI

Article

Enhanced Removal of Non-Steroidal Inflammatory Drugs from Water by Quaternary Chitosan-Based Magnetic Nanosorbents

Sofia F. Soares [ID]**, Tito Trindade** [ID] **and Ana L. Daniel-da-Silva *** [ID]

CICECO-Aveiro Institute of Materials, Department of Chemistry, University of Aveiro, 3810-193 Aveiro, Portugal;
sofiafsoares@ua.pt (S.F.S.); tito@ua.pt (T.T.)
* Correspondence: ana.luisa@ua.pt; Tel.: +351-234-401-518

Abstract: Non-steroidal anti-inflammatory drugs (NSAIDs) are among the most common pharmaceuticals used worldwide. They are widely detected in natural waters due to their persistence in wastewater treatment, and their removal is desirable in wastewater management. As a contribution to tackle this challenge, this study explores magnetic quaternary chitosan-based nanosorbents for the effective magnetically assisted removal of three NSAIDs (diclofenac, naproxen, and ketoprofen) from water. Toward this goal, silane groups were grafted onto the backbone of trimethyl chitosan through the reaction with an epoxide functionalized silane. Once silanized, the modified chitosan was employed to coat Fe_3O_4 nanoparticles. The prepared materials were characterized using FTIR spectroscopy and solid-state ^{29}Si and ^{13}C NMR spectroscopy, which confirmed the encapsulation of Fe_3O_4 nanoparticles with a hybrid siliceous material enriched in trimethyl chitosan. The effect of the initial NSAIDs concentration, pH, and contact time in the adsorption behavior was investigated. The kinetic data were well described by the pseudo-second-order kinetic model, indicating a chemisorption mechanism. The maximum adsorption capacities estimated from the Langmuir model were 188.5 mg/g (0.5925 mmol/g), 438.1 mg/g (1.7371 mmol/g), and 221.5 mg/g (0.8710 mmol/g) for diclofenac, naproxen, and ketoprofen, respectively. These adsorption capacities are higher than those of most reported sorbents, indicating the potential of these biosorbents to remove the selected NSAIDs using low-energy magnetically assisted separation.

Keywords: non-steroidal anti-inflammatory drugs; trimethyl chitosan; magnetic particles; adsorption

1. Introduction

Water pollution is one of the most critical environmental problems that the world urgently needs to address, since clean water is vital for every living organism [1]. There has been an increasing interest in emerging contaminants, such as pharmaceutically active compounds [2]. In the European Union (EU), about 3000 different substances are used for human medication purposes that are highly persistent in the environment and are of toxicological concern [3]. These chemicals are considered emerging pollutants because their discharge limits in the environment still remain unregulated or are in the process of regularization [4,5]. Non-steroidal anti-inflammatory drugs (NSAIDs) are among the most frequently used pharmaceuticals and are included in the watch list of compounds in the EU related to the top 10 persistent pollutants [6]. NSAIDs encompass an extensive range of pharmaceuticals used to treat pain and inflammation in different arthritic and post-operative situations [6,7]. Among the NSAIDs, diclofenac (DCF), naproxen (NAP), and ketoprofen (KET) are recurrently detected in the environment as trace contaminants [1,8,9]. NSAIDs undergo several processes during wastewater treatment, but they are not entirely removed from water using conventional procedures [6,10]. This contributes to the occurrence of high levels of NSAIDs in aquatic environments, reaching values as high as μg/L concentration at multiple locations worldwide [6,11].

Several treatment methods such as activated carbon filtration, reverse osmosis, flocculation, and ozonation and advanced technologies including membrane bioreactors and ad-

vanced oxidation processes have been proposed to remove pharmaceuticals from wastewater [9,12–15]. The field application of most of these methods is limited by complex processes, high-energy consumption, and consequently high costs. In the search for greener and more sustainable removal processes, of easy operation and affordable cost, polysaccharides offer several advantages as promising candidates for adsorption processes because they are biopolymers that are naturally available, biodegradable, and relatively low-cost [16]. Furthermore, they contain numerous functional groups in their structure that can interact with pollutants dissolved in water. However, polysaccharide-based sorbents are challenging to separate from treated water, a limitation that has restrained their use [16]. To improve the adsorption properties and overcome these drawbacks, some efforts have been undertaken to develop organic–inorganic hybrids by grafting the polysaccharides to water-insoluble inorganic substrates [17–20]. Because of the mild conditions provided by sol–gel chemistry, this route is highly attractive for incorporating biopolymers [21]. These methods employ functional alkoxysilanes as linkers between the siliceous shells and the biopolymer, for obtaining hybrid materials in which such phases are strongly linked. Typically, these silane coupling agents have a functional group selected to react with the biopolymer, and hydrolyzable alkoxy groups that form covalent bonds with the siliceous component [22–25].

Chitosan is a natural amino-polysaccharide derived from chitin, which is one of the most abundant biopolymers in nature [26]. The existence of primary amine and hydroxyl groups in its structure allows for chemical modifications, improving their solubility and providing reactive groups for covalent bonding to an inorganic substrate, such as amorphous silica [27]. For example, chitosan was chemically modified into multi-functional sorbents to accomplish certain requirements for specific applications [28]; *N,N,N*-trimethyl chitosan (TMC), a quaternary hydrophilic derivative of chitosan, has attracted considerable attention because it contains quaternary ammonium moieties ($-N^+(CH_3)_3$) in its backbone [29,30]. The cationic nature is very appealing and led to the development of novel sorbents with the ability to interact with negatively charged pollutants [29].

In the past few years, colloidal magnetic nanoparticles have been proposed as sorbents for water treatment applications due to their magnetic features, large surface area, and facile water dispersibility [16,31,32]. Magnetic nanoparticles are easily and quickly separated from treated water in the presence of an external magnetic field gradient, representing an advantage in relation to non-magnetic sorbents. Iron oxide nanoparticles are the most used in research to treat polluted water due to their low cost and moderate environmental impact [16]. These magnetic nanoparticles can be applied to remove contaminants from water provided they have been surface modified with an adequate coating, which can be either inorganic or organic in nature [16]. The enhancement of the adsorptive capacity of magnetic nanoparticles and improved selectivity towards target pollutants can be achieved by chemical functionalization of the particles' surfaces with biopolymers.

This research aimed to explore a new chemical route for the surface modification of colloidal magnetic nanoparticles in which siliceous shells of trimethyl chitosan (TMC) have been modified with an epoxide functionalized silane coupling agent. These new magnetic nanosorbents were investigated for the adsorptive removal of three selected NSAIDs (diclofenac, naproxen, and ketoprofen) from water. Additionally, the kinetics and the equilibrium of the adsorption process were studied to understand the adsorption behavior and mechanism involved.

2. Materials and Methods

2.1. Chemicals

The pharmaceuticals used in the adsorption studies were sodium diclofenac salt ($C_{14}H_{10}Cl_2NNaO_2$, Alfa Aesar, Kandel, Germany, >98%), sodium naproxen ($C_{14}H_{13}NaO_3$, Sigma-Aldrich, Steinheim, Germany, 98%–100%), and ketoprofen ($C_{16}H_{14}O_3$, Sigma-Aldrich, >98%). Trimethyl chitosan was supplied by Henan Tianfu Chemical Co., Ltd. (Zhengzhou, China) and used as received (degree of quaternization: 15.3%). Ferrous sulfate

heptahydrate ($FeSO_4 \cdot 7H_2O$, Panreac, Barcelona, Spain, >99%), potassium hydroxide (KOH, LabChem, Zelienople, PA, USA, >86%), and potassium nitrate (KNO_3, Sigma-Aldrich, >99%) were used in the synthesis of magnetite nanoparticles. Ethanol (CH_3CH_2OH, Panreac, >99%) and methanol (CH_3OH, VWR, Radnor, PA, USA, >99%) were used to wash the prepared materials. 3-(glycidyloxypropyl)trimethoxysilane (GPTMS, $C_9H_{20}O_5Si$, Sigma-Aldrich, >98%) was used as a silane coupling agent. *N,N*-dimethylformamide ($HCON(CH_3)_2$, Carlo Erba Reagents, Peypin, France, >99%) was used as a solvent. Tetraethyl orthosilicate (TEOS, $Si(OC_2H_5)_4$, Sigma-Aldrich, >99%) was used as a silica precursor. Ammonia solution (NH_4OH, Riedel-de-Häen, Hanover, Germany, 25%) was used as a base catalyst. All solutions were prepared in ultra-pure water (0.22 μm filter, Milli-Q, Millipore, Darmstadt, Germany).

2.2. Derivatization of the Quaternary Chitosan

Trimethyl chitosan (TMC) was modified by reaction with the alkoxysilane coupling agent GPTMS [19,20,33]. Hence, TMC (1 g) was previously dried at 30 °C for 24 h, and the reaction with GPTMS (5.2 mmol, 1.24 mL) was performed using dry *N,N*-dimethylformamide (13 mL) as solvent. The reaction was conducted at 100 °C, under a dry nitrogen atmosphere, with stirring at 500 rpm and over 24 h. The obtained material, hereafter named TMC/GPTMS, was washed thoroughly with dry methanol and dry ethanol and finally dried at room temperature.

2.3. Synthesis of Magnetic Bio-Hybrid Sorbent

The magnetic core was synthesized by oxidative hydrolysis of $Fe_2SO_4 \cdot 7H_2O$ in alkaline conditions to obtain magnetite (Fe_3O_4) nanoparticles (Supporting Information) [34]. Then the magnetic core was coated using the sol–gel method by adding a mixture of the silica precursor (TEOS) with the derivatized chitosan (TMC/GPTMS). Briefly, for the coating, an ethanolic solution (38 mL) containing Fe_3O_4 nanoparticles (40 mg) was kept immersed in an ice bath under sonication (horn Sonics, Vibracell) for 15 min. Next, the ammonia solution (2.4 mL), TEOS (0.406 mL), and TMC/GPTMS (0.3 g) were slowly added, and the reaction was maintained for 2 h under sonication in an ice bath. After the reaction, the resulting magnetic biosorbent was collected by magnetic separation using an NdFeB magnet and washed six times with ethanol. The particles were dried at room temperature, and the quaternary chitosan magnetic biosorbent ($Fe_3O_4@SiO_2$/TMC/GPTMS) was obtained.

2.4. Synthesis of Non-Magnetic Quaternary Chitosan Particles

Non-magnetic quaternary chitosan particles (SiO_2/TMC/GPTMS) were also prepared by employing a similar method but in the absence of Fe_3O_4 nanoparticles. In the synthesis, 0.3 g of TMC/GPTMS and 0.406 mL of TEOS were added to a mixture of 0.9 mL of deionized water, 8.5 mL of ethanol, and 0.15 mL of ammonia [35]. The reaction was stirred (500 rpm) at RT for 24 h. Then, the particles were washed five times with deionized water and one time with dry ethanol, separated by centrifugation (10 min at 13,300 rpm), and dried. For complementary studies using solid state NMR spectroscopy (Bruker, Billerica, MA, USA), SiO_2 particles were also prepared by using the Stöber method (Supporting Information) [36].

2.5. Characterization of Materials
2.5.1. X-ray Powder Diffraction

The crystalline structure of the produced materials was evaluated by X-ray powder diffraction (XRD). The XRD data were collected using a PANalytical Empyrean X-ray diffractometer (Malvern, Worcestershire, UK) equipped with a Cu Kα monochromatic radiation source at 45 kV/40 mA.

2.5.2. Fourier Transform Infrared Spectroscopy

Fourier transform infrared (FTIR) spectra of the materials were acquired over the range of 4000–450 cm^{-1} using a Bruker Optics Tensor 27 spectrometer (Bruker, Billerica, MA, USA) coupled to a horizontal attenuated total reflectance (ATR) cell. The samples were placed on the ATR crystal, and 256 scans were acquired at 4 cm^{-1} resolution.

2.5.3. Transmission and Scanning Electron Microscopy

The morphology of the produced materials was analyzed by transmission electron microscopy (TEM) and scanning electron microscopy (SEM). Transmission electron microscopy was performed using a Hitachi H-9000 TEM microscope (Chiyoda, Tokyo, Japan) carried out at an accelerating voltage of 300 kV. A drop (10 μL) of a diluted suspension of the particles in ethanol was placed on a copper grid with a lacey amorphous carbon film and left to dry before TEM analysis. Scanning electron microscopy was performed using a Hitachi SU-70 instrument at 15 kV. For SEM analysis, the samples were prepared by placing an aliquot of a dilute suspension of particles in ethanol on a glass slide, which was glued to the sample holder using double-sided carbon tape, and then coated with carbon.

2.5.4. Elemental Analysis, Specific Surface Area, and Pore Volume

The elemental analysis of carbon, hydrogen, nitrogen, and sulfur was performed using a Leco Truspec-Micro CHNS 630-200-200 (Leco, Saint Joseph, MI, USA). The specific surface area of the particles was assessed by nitrogen adsorption/desorption measurements using a Gemini V2.0 Micromeritics instrument (Micromeritics, Norcross, GA, USA). The materials were first outgassed overnight at 80 °C/1.5 bar, and then adsorption and desorption isotherms were conducted at liquid nitrogen temperature (−196 °C). The specific surface area was determined using the Brunauer–Emmett–Teller (BET) equation for relative pressures (P/P$_0$) up to 0.3. The pore volume was evaluated from the adsorption amount using the Barret–Joyner–Halenda (BJH).

2.5.5. Zeta Potential

The surface charge of the colloidal nanoparticles was assessed by zeta potential measurements in a Zetasizer Nano ZS instrument (Malvern Instruments) (Malvern, Worcestershire, UK) that uses a HeNe laser operating at 633 nm and a scattering detector at 173°. The measurements were performed in aqueous suspensions of the particles using a disposable folded capillary cell.

2.5.6. Nuclear Magnetic Resonance Spectroscopy

The ^{13}C cross-polarization (CP)/magic-angle spinning (MAS) nuclear magnetic resonance (NMR) and ^{29}Si MAS/CP MAS NMR spectra were recorded on a Bruker Avance III 400 MHz (9.4 T) spectrometer(Bruker, Billerica, MA, USA) at 79.49 and 100.61 MHz, respectively. ^{13}C CP/MAS NMR spectra were acquired with 3.65 μs ^{1}H 90° pulses, 1.5 ms contact time, a recycle delay of 5 s, and at a spinning rate of 9 kHz. ^{29}Si MAS NMR spectra were recorded with 4.5 μs ^{1}H 90° pulses, a recycle delay of 60 s, and at a spinning rate of 5 kHz. The chemical shifts are quoted in ppm relative to tetramethylsilane (TMS).

2.6. Batch Adsorption Experiments

Individual aqueous solutions of diclofenac sodium (DCF), naproxen sodium (NAP), and ketoprofen (KET), with the required concentrations, were prepared using ultra-pure water. The DCF, NAP, and KET concentrations were determined spectrophotometrically using a Jasco U 560 UV–VIS spectrophotometer, measuring the maximum absorbance at 276, 230, and 260 nm, respectively. The calibration curves were obtained from the analysis of the spectra obtained at distinct NSAID concentrations: DCF (0.12–12.0 mg/L), NAP (0.12–3.0 mg/L), and KET (0.12–12.0 mg/L) (Figure S1, Supporting Information). The structures and characteristics of NSAIDs are shown in Table S1 (Supporting Information). The experiments were performed in glass vials, in which an exact amount of the magnetic

biosorbent (0.5 mg/mL dosage) was placed in contact with solutions with known DCF, NAP, and KET concentration. The NSAID solutions containing the magnetic biosorbent were continuously stirred in an orbital shaker incubator (IKA, Staufen, Germany, KS 4000i control) at 200 rpm under controlled temperature (25.0 $\pm$ 1.0 °C) over a specific time (0 min to 300 min) in dark conditions. After adsorption for a pre-determined contact time, the biosorbent was magnetically separated using a NdFeB magnet, and the concentration of the corresponding pharmaceutical (C_t) in the supernatant was assessed by UV–VIS spectroscopy (GBC Scientific Equipment, Hampshire, IL, USA). The percentage of removal of each NSAIDs was calculated using Equation (1), where C_0 is the initial concentration (mg/L).

$$\text{R (\%)} = \frac{(C_0 - C_t)}{C_0} \times 100 \tag{1}$$

Additionally, control experiments (pharmaceutical solution without the sorbent) were carried out simultaneously with adsorption experiments.

2.6.1. Effect of pH on the Removal of NSAIDs

DCF, NAP, and KET solutions (50 mg/L), with distinct pH values (5, 6, 7, 8, and 9), were prepared by adjusting the pH with an appropriate amount of NaOH (0.01 M) or HCl (0.01 M). The adsorption experiments were then conducted using 0.5 mg/mL of sorbent in each case. The mixtures were shaken continuously at 30 rpm for 5 h to ensure that the adsorption equilibrium was achieved. Then, the magnetic biosorbent was separated magnetically from the solution, and DCF, NAP, and KET concentrations in the supernatant were assessed by UV–VIS spectrophotometry.

2.6.2. Kinetics and Equilibrium Adsorption Studies

The adsorption kinetics of single DCF, NAP, and KET solutions with different concentrations (10, 50, and 100 mg/L) were prepared, and the pH was adjusted to 5. An appropriate amount of the magnetic biosorbent was added to the mixture (0.5 mg/mL), and the adsorption process was conducted. The mixtures were shaken, and aliquots of 1 mL were collected along the time (during 5 h, 300 min) at room temperature (25.0 $\pm$ 1.0 °C). The amount of pharmaceutical adsorbed at each time t (q_t, mg/g) was determined by Equation (2):

$$q_t = (C_0 - C_t) \times \frac{V}{m} \tag{2}$$

where C_0 (mg/L) is the initial concentration (mg/L), C_t (mg/L) is the pharmaceutical concentration in the aqueous phase at time t (min), V (L) is the volume of solution, and m (mg) is the mass of the magnetic biosorbent.

Equilibrium adsorption studies were performed by dispersing 0.5 mg/mL of magnetic biosorbent, in DCF, NAP, and KET aqueous solutions, with distinct initial concentrations (ranging from 5 to 350 mg/L) at pH = 5. The experiments were conducted for 5 h (300 min) at room temperature (25.0 $\pm$ 1.0 °C). The amount of DCF, NAP, and KET adsorbed at equilibrium (q_e, mg/g) was assessed by UV–VIS spectroscopy and calculated using Equation (2) for $C_t = C_e$, where C_e (mg/L) is the concentration of DCF, NAP, and KET at equilibrium.

3. Results and Discussion

3.1. Materials Characterization

3.1.1. XRD Analysis

The powder X-ray diffraction (XRD) pattern of the particles used as cores (Figure 1a), along with the labelling of the respective Miller indices, indicated the presence of magnetite (Fe_3O_4) with cubic inverse spinel structure (JCPDS file No. 19-0629) [37]. A similar XRD pattern was observed for the Fe_3O_4@SiO_2/TMC/GPTMS particles, confirming that after surface modification, the composition of the core of the particles was maintained as Fe_3O_4. The XRD of the Fe_3O_4@SiO_2/TMC/GPTMS particles also showed a broad peak around 23° that is characteristic of short-range order in amorphous SiO_2, in agreement with the

presence of the siliceous network coating the magnetic cores [38]. These Fe_3O_4 particles are ferrimagnetic and exhibit a small magnetization hysteresis loop at room temperature with a saturation magnetization of 83 emu/g [19].
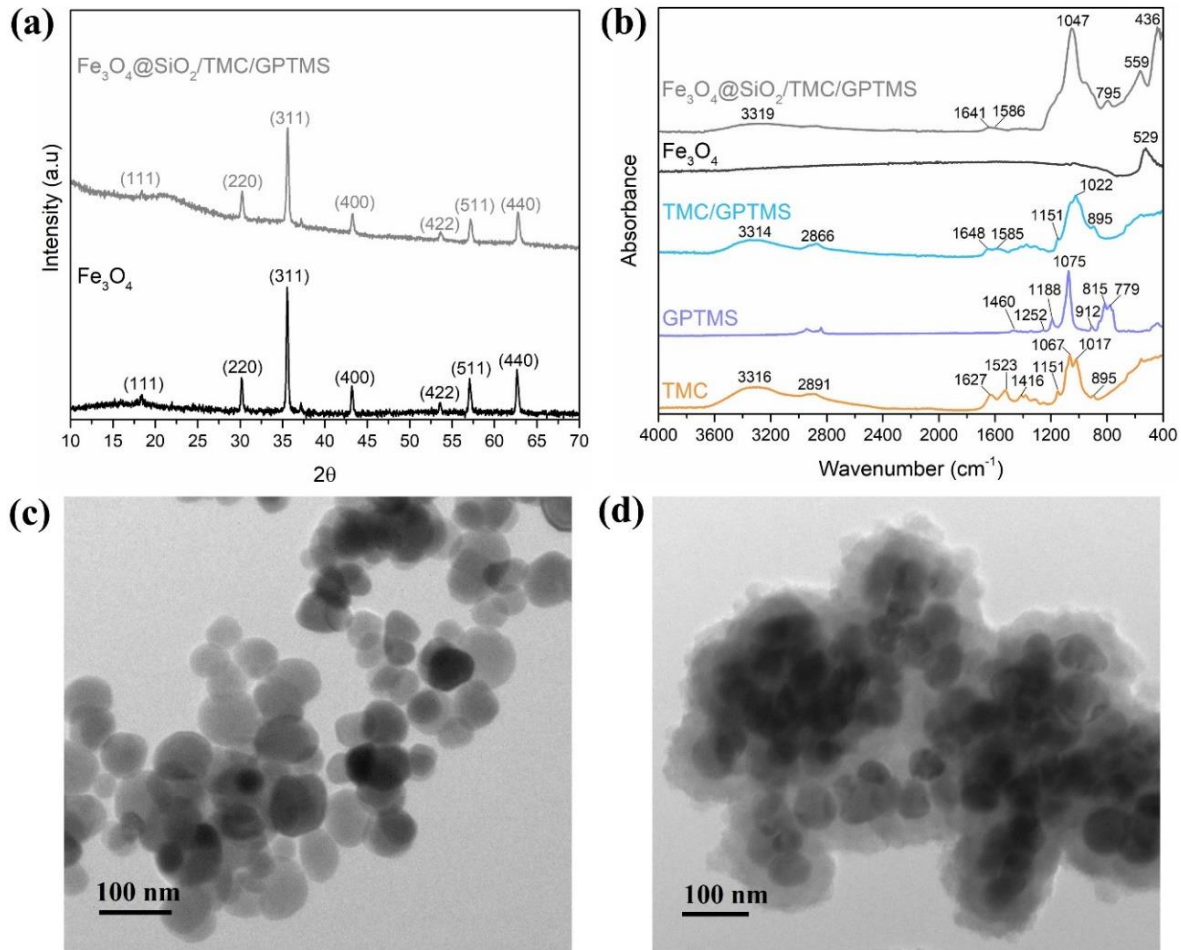

Figure 1. (**a**) Powder XRD patterns of Fe_3O_4 and $Fe_3O_4@SiO_2$/TMC/GPTMS particles; (**b**) ATR-FTIR spectra of TMC, GPTMS, TMC/GPTMS, Fe_3O_4, and $Fe_3O_4@SiO_2$/TMC/GPTMS materials; and TEM images of (**c**) Fe_3O_4 and (**d**) $Fe_3O_4@SiO_2$/TMC/GPTMS particles.

3.1.2. FTIR and TEM Results

The FTIR spectrum of the Fe_3O_4 particles (Figure 1b) showed the characteristic band at 529 cm^{-1} assigned to the Fe–O stretching vibration [39]. This band was also visible at 559 cm^{-1} in the spectrum of $Fe_3O_4@SiO_2$/TMC/GPTMS particles, although it was shifted to higher wavenumbers. FTIR analysis of the coated particles was challenging because the main vibrational bands of TMC and the siliceous network may overlap. The FTIR spectrum of TMC showed bands at approximately 3316 cm^{-1} attributed to –OH bonds, at 2891 cm^{-1} ascribed to asymmetrical stretching of C–H bonds, and peaks at 1627 and 1523 cm^{-1} belonging to C–O stretching (amide I) and N–H bending (amide II) vibrations, respectively [40]. Moreover, the band at 1416 cm^{-1} was assigned to the characteristic absorption of N–CH$_3$ groups in TMC [41]. Additionally, the intense bands between 1000 and 1200 cm^{-1} were ascribed to C–O vibrations in the polysaccharide backbone [33]. In the preparation of TMC/GPTMS, both hydroxyl and amine groups of TMC can react with the epoxide groups of the alkoxysilane GPTMS to yield ether ($-CH_2OCH_2-$) and secondary amine ($-CHNHCH_2-$) covalent bonds, respectively (Figure 2). In the FTIR spectrum of GPTMS (Figure 1b), the band at 1460 cm^{-1} is associated with the deformation vibrational mode of the methylene groups of the propyl unit [42,43]. The band at 1252 cm^{-1} was

due to the epoxide ring stretching vibration, and the band at 1188 cm^{-1} was ascribed to the C−H deformation mode of the Si−O−CH$_3$ [42–44]. The C−O stretching vibration of the epoxide ring could be observed at 912 cm^{-1}, and the bands at 1075 cm^{-1}, 815 cm^{-1}, and 779 cm^{-1} corresponded to the stretching and bending vibrations of the Si−O−C bonds of GPTMS [42,43,45]. In the TMC/GPTMS spectrum, the absence of the band of the epoxide ring could be evidence for epoxide ring opening upon reaction with TMC [46–48]. The amide bands of TMC were retained and appeared shifted to higher wavenumbers (1627–1648 and 1585 cm^{-1} for C=O and N–H bending, respectively). This may be attributed to changes in the H-bonding network in the TMC/GPTMS. Although the FTIR results are not conclusive to clearly discern the mechanism for the reaction between TMC and GPTMS, the results suggest the formation of covalent bonding through the reaction of the epoxide ring of GPTMS. The FTIR spectrum of Fe$_3$O$_4$@SiO$_2$/TMC/GPTMS particles also displayed the vibrational bands expected for a material comprising a siliceous network. This inorganic phase gives FTIR bands at 795 cm^{-1} and 446 cm^{-1} that can be assigned to symmetric Si–O–Si stretching and O–Si–O deformation modes of amorphous silica, respectively [20,33]. Moreover, the presence of a broad band centered at 1047 cm^{-1} can result from overlapped vibrational contributions of the trimethyl chitosan and amorphous silica [20,33].
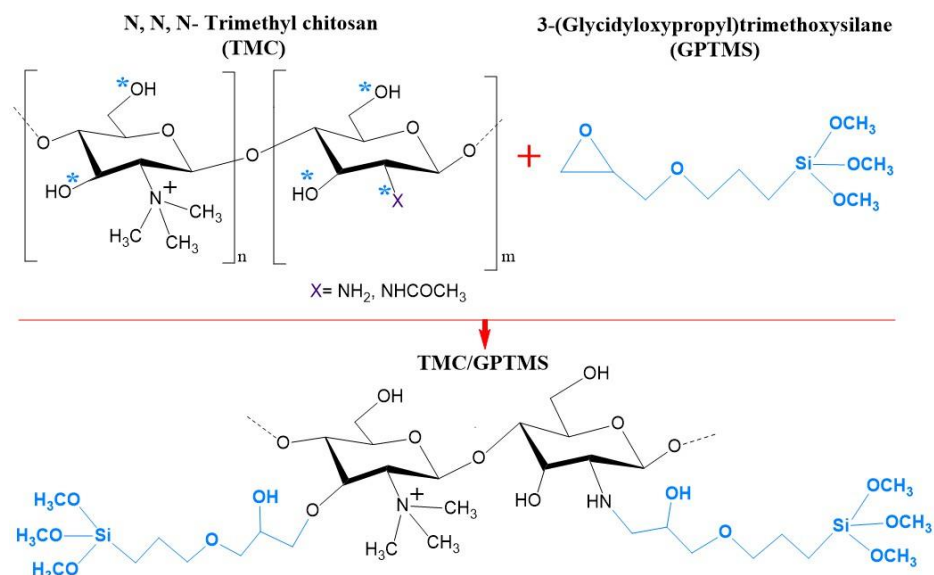

Figure 2. Schematic representation of the reaction between the hydroxyl (−OH) and/or amine (−NH$_2$) groups of *N,N,N*-trimethyl chitosan (TMC) with the epoxide groups of 3-(glycidyloxypropyl)trimethoxysilane (GPTMS). The reactive target sites are indicated with *.

The resulting particles were composed of a magnetite spheroidal core (56 ± 11 nm) coated by amorphous shells with irregular surfaces (Figure 1c,d). The thickness of the shells was around 37 ± 6 nm. The XRD and FTIR results and the TEM images confirmed the encapsulation of the Fe$_3$O$_4$ particles. Note that the TEM image provided was representative of the sample, always showing denser nanoparticles (magnetite) surrounded by a material with lower image contrast (biopolymer/silica material), resulting in small aggregates with several magnetic cores.

3.1.3. Specific Surface Area and Elemental Analysis

The BET specific surface area decreased from 27.4 m^2/g in Fe$_3$O$_4$ to 13.6 m^2/g in Fe$_3$O$_4$@SiO$_2$/TMC/GPTMS particles (Table 1), which is consistent with an increase of the average particle size due to the formation of the outer hybrid shells. Table 1 shows the elemental microanalysis results of the prepared materials. As expected, the Fe$_3$O$_4$ particles revealed negligible carbon (<0.2%) and nitrogen (<0.04%) contents. In contrast,

the Fe$_3$O$_4$@SiO$_2$/TMC/GPTMS particles had a carbon content of 30 wt% and a relevant nitrogen amount (5.9 wt%), confirming the incorporation of the organic (TMC) component in the final particles.

Table 1. Compositional and structural properties of the materials: elemental analysis, particle diameter, BET surface area, and pore volume.

Sample	C (%) [a]	H (%) [a]	N (%) [a]	D (nm) [b]		S$_{BET}$ (m^2/g) [c]	V$_p$ (cm^3/g) [c]
				Core	Shell		
TMC	32.8	5.6	5.9	–	–	–	–
TMC/GPTMS	35.8	6.8	6.8	–	–	–	–
Fe$_3$O$_4$	0.2	0.06	0.04	56 ± 11	–	27.4	0.066
Fe$_3$O$_4$@SiO$_2$/TMC/GPTMS	30.3	5.7	5.9	56 ± 11	37 ± 6	13.6	0.014

[a] Carbon, hydrogen, and nitrogen content assessed by elemental microanalysis; [b] particle diameter measured by TEM; [c] BET surface area (S$_{BET}$) and pore volume (V$_p$) assessed by N$_2$ sorption.

3.1.4. NMR Analysis

Solid-state NMR spectroscopy analysis of the non-magnetic quaternary chitosan particles (SiO$_2$/TMC/GPTMS) was performed to inquire about the shells' chemical nature of the Fe$_3$O$_4$@SiO$_2$/TMC/GPTMS particles. A brief characterization of SiO$_2$/TMC/GPTMS particles by SEM and FTIR spectroscopy is included in Figure S2 (Supporting Information). Figure 3a shows the ^{13}C CP/MAS NMR spectra for TMC and SiO$_2$/TMC/GPTMS particles, and the corresponding chemical-shift assignments are listed in Table S2 (Supporting Information). The ^{13}C NMR spectrum of TMC showed the following evidences: δ = 24.3 ppm attributed to the carbon atom of the methyl moieties of the acetyl groups; δ = 54.8 ppm, which correspond to carbon atoms of *N,N*-dimethylated groups; δ = 55.2 ppm attributed to carbon atoms of *N,N,N*-trimethylated groups; δ = 57.8 ppm, where two overlapped signals were observed and ascribed to carbon C$_6$ and C$_2$; δ = 71.2 ppm, representing the carbon atoms in the O-methylated groups; δ = 74.7 ppm assigned to carbons C$_5$ and C$_3$; δ = 81.1 ppm ascribed to the carbon C$_4$; δ = 99.7 ppm assigned to carbon C$_1$; and finally δ = 173.8 ppm that corresponds to the carbon of carbonyl of acetyl group [49,50]. The ^{13}C NMR spectrum of SiO$_2$/TMC/GPTMS showed the resonances associated with the carbons of GPTMS that were overlapped with the NMR peaks assigned to the carbon atoms of TMC and that were observed in the range δ = 22.8–173.8 ppm. The methoxy groups (Si–O–CH$_3$) associated with GPTMS are usually identified by a ^{13}C resonance at δ = 50 ppm. However, this resonance was absent, suggesting that the hydrolysis of GPTMS to form silanol groups proceeded to completion [23]. The signals of the carbon atoms C$_a$ and C$_b$ of the Si-bonded propyl chain linked to GPTMS at δ = 22.8 ppm were overlapped with the signal of the carbon of the methyl moieties of the acetyl groups, which were attributed to the reaction of epoxide ring with the primary amine of TMC (–NH$_2$) to form a secondary amine [24]. Due to many different C–O species, the spectrum was saturated with resonances in the range of 50–120 ppm, making difficult the assignment of the resonances of C$_c$, C$_d$, C$_e$, and C$_f$ in this region. Nevertheless, the literature concerning the reaction of different biopolymers with GPTMS suggests that the resonances of the carbons C$_c$, C$_d$, C$_e$, and C$_f$ might be assigned in this region [51–53].

^{29}Si NMR spectroscopy was used to provide further insight into the structure of hybrid materials. The ^{29}Si MAS NMR and ^{29}Si CP/MAS NMR spectra of the non-magnetic SiO2/TMC/GPTMS particles are shown in Figure 3b,c, respectively. For comparison, the NMR spectra of amorphous SiO$_2$ particles prepared using the same approach but in the absence of TMC (SEM and FTIR results were included in Figure S2, Supporting Information) were also included in Figure 3b,c. A specific region could be clearly observed from δ = −90 to −120 ppm, corresponding to the silica Q species. The Q species describes the connectivity of the silica network, and the Q^n denotes a silicon atom with n bridging oxygens (Figure 3d) [54]. Therefore, a higher value of n in Q species indicates a more connected silica network. From the ^{29}Si MAS NMR spectrum of SiO$_2$/TMC/GPTMS, it

was clear that the Q^2 ($\delta = -91.9$ ppm), Q^3 ($\delta = -101.2$ ppm), and Q^4 ($\delta = -111.3$ ppm) structures were the dominant Q species, in accordance with the literature (Figure 3b) [54]. The degree of condensation of the silica network could be obtained using the fraction of silanol groups (($Q^2 + Q^3$)/Q^4) calculated from the ^{29}Si MAS NMR spectra, and is given in Table S2, Supporting Information. The degree of condensation was 0.52 in SiO_2 particles and decreased to 0.48 in the SiO_2/TMC/GPTMS particles. Since the degree of condensation decreased, it means evidence for the covalent bonding of the precursor TMC/GPTMS with the surface of the particles [35]. From the ^{29}Si CP/MAS NMR spectrum of SiO_2/TMC/GPTMS (Figure 3c), two distinct regions could be clearly observed from $\delta = -50$ to -70 ppm and from $\delta = -90$ to -120 ppm, corresponding to the silica T and Q species, respectively. The amount of T species indicates the degree of cross-linking between GPTMS and the silica network. T^n denotes a silicon atom bonded to carbon with n bridging oxygens (–Si–O–Si–) [24]. Therefore, a higher value of n in T and Q species indicates a more connected silica network. From the ^{29}Si CP/MAS NMR spectra (Figure 3c) it was possible to observe that the Q^3 and Q^4 structures were the dominant Q species in the SiO_2/TMC/GPTMS particles with no Q^1 species detected, implying a highly condensed silica network [24,54]. Moreover, the ^{29}Si CP/MAS NMR spectrum of SiO_2/TMC/GPTMS particles showed two resonances ascribed to the T^2 ($\delta = -57.6$ ppm) and T^3 ($\delta = -64.2$ ppm) sites [55]. Additionally, the absence of T^1 species indicated that the alkoxy portion of the GPTMS molecules underwent a high degree of condensation, confirming the covalent bonding of TMC/GPTMS to the siliceous network.

3.2. Adsorption Studies

3.2.1. Influence of pH and Adsorption Mechanism

The pH of the solution is a key factor in the adsorption process and interactions at the sorbent–sorbate interface. It influences the surface chemistry of the sorbent and the speciation of the solutions. The pKa range of the three targeted NSAIDs was between 4.00 and 4.45 (pKa DCF = 4.00; pKa NAP = 4.19; pKa KET = 4.45) [7], as shown in Figure 4a–c. The selected NSAIDs are classified as weak acid compounds, and thus the pH will affect their chemical speciation in solution. At pH < pKa, the NSAIDs are mainly protonated (neutral), while at pH > pKa the NSAIDs are deprotonated (negatively charged). Measurement of zeta potential values of the Fe_3O_4@SiO_2/TMC/GPTMS particles as a function of pH was also performed to provide information on the surface charge of the sorbent (Figure 4d). The point of zero charge (pH$_{pzc}$) is the pH in which the net charge on the sorbent surface is zero, and it was found to be between pH = 8 and 9, which means that at pH < pH$_{pzc}$ the surface was positively charged (Figure 4d) and could interact electrostatically with deprotonated NSAIDs species. At pH values not higher than 8, the particles presented positive zeta potentials due to the contribution of cationic trimethylammonium groups ($-N^+(CH_3)_3$) from TMC present at the particles' surfaces. Adsorption of DCF, NAP, and KET showed identical pH-dependent patterns (Figure 4d). This indicates that these NSAIDs may undergo the same type of interactions with the surface of Fe_3O_4@SiO_2/TMC/GPTMS particles. As shown in Figure 4d, high adsorption capacity was observed at pH = 5 for DCF, NAP, and KET, and then the subsequent adsorption experiments were performed at this pH. At this pH, the particles are positively charged, and the NSAIDs are mainly in the deprotonated form, which promotes the electrostatic interactions and increase the adsorption capacity [56]. When the pH increased from 5 to 9, the adsorption capacity (q_t) decreased for all the NSAIDs tested, most likely because the surface charge of the nanoparticles also decreased. At pH = 9 the NSAIDs and the surface of the particles were negatively charged, and repulsive forces could occur. However, the particles still adsorbed NSAIDs, indicating that electrostatic interactions are not the only mechanisms that govern the adsorption at this pH.

There are several possible mechanisms for the adsorption of NSAIDs onto the Fe_3O_4@SiO_2/TMC/GPTMS particles: (i) electrostatic interactions between the cationic trimethylammonium groups from TMC and the carboxylate groups of the NSAIDs molecules [57,58]; (ii) H-bonding

interactions among the NSAIDs (carboxyl, amine, and ester groups) with the hydroxyl groups of trimethyl chitosan [58,59]; and (iii) hydrophobic interactions in which the hydrophobic dimethylated groups ($-N(CH_3)_2$) of trimethyl chitosan can capture the NSAID molecules [59–61]. Previous studies have explained the adsorption of NSAIDs on other sorbents based on hydrogen bonding [59,60]. Taking into account the results in Figure 4d, at pH = 9, the adsorption capacity of each NSAID towards $Fe_3O_4@SiO_2/TMC/GPTMS$ particles decreased in the order DCF > NAP > KET. The extent of the interaction through hydrogen bonding has been well explained based on two factors: differences in the chemical structures of each NSAIDs, and the interactions between each functional group present in the NSAIDs [60,62]. As can be seen by the molecular structures of DCF, NAP, and KET (Table S1, Supporting Information), these molecules showed three bonding sites each. Hydrogen bonding increased as the accessibility of the available sites for interaction increases in each NSAID molecule. Furthermore, among the NSAIDs tested, DCF presented a higher affinity towards sorbent particles, most likely because it contains both H-donor (amine) and H-acceptor (oxygen-containing) functional groups that can establish H-bonds with $Fe_3O_4@SiO_2/TMC/GPTMS$ particles [60]. In the case of NAP, the oxygen of the methoxy group may lead to more hydrogen bonding than the keto-group in KET [60].
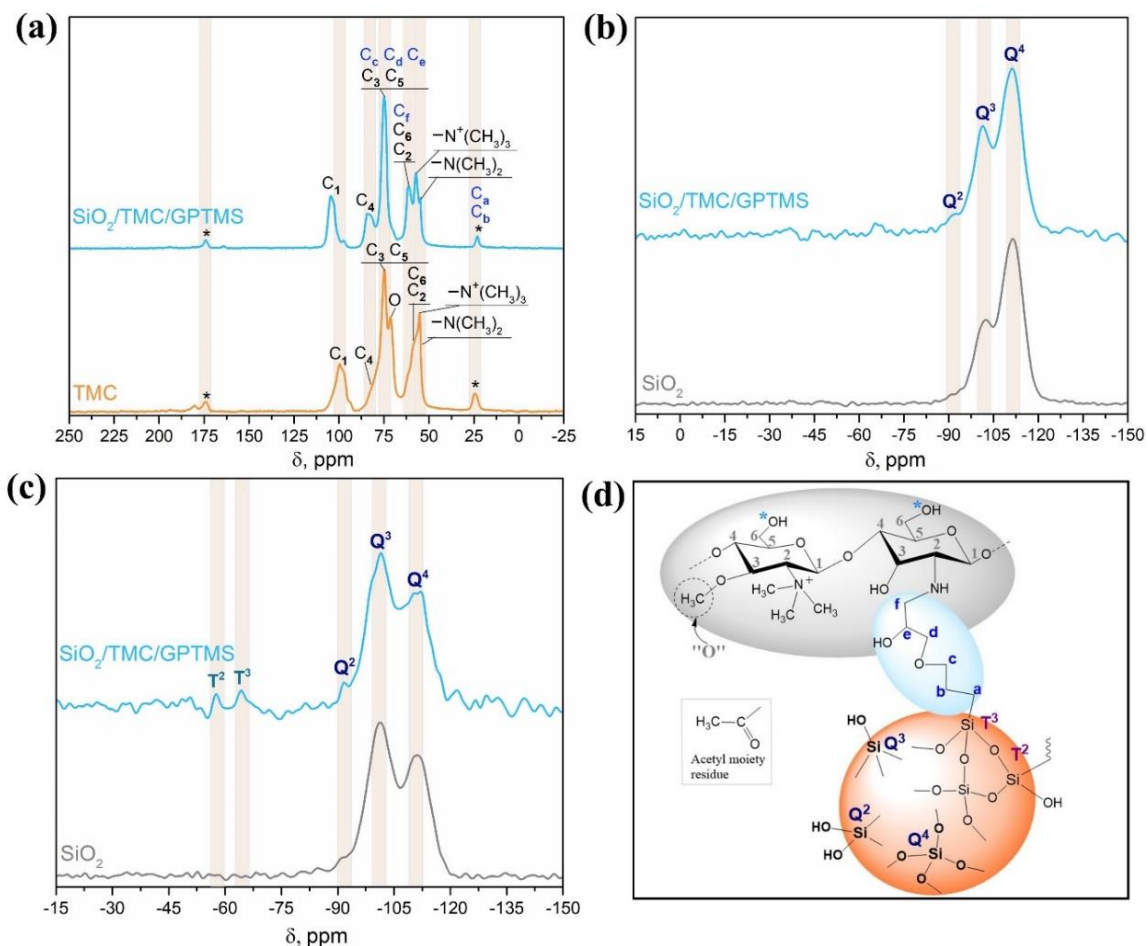

Figure 3. (**a**) ^{13}C CP/MAS NMR spectra of TMC and $SiO_2/TMC/GPTMS$ hybrid particles; (**b**) ^{29}Si MAS NMR spectra and (**c**) ^{29}Si CP/MAS NMR spectra of SiO_2 and $SiO_2/TMC/GPTMS$ particles; and (**d**) schematic representation of $SiO_2/TMC/GPTMS$ particles with the labelling of Si sites according to NMR spectroscopy notation (acetyl groups are not represented in the TMC molecule).
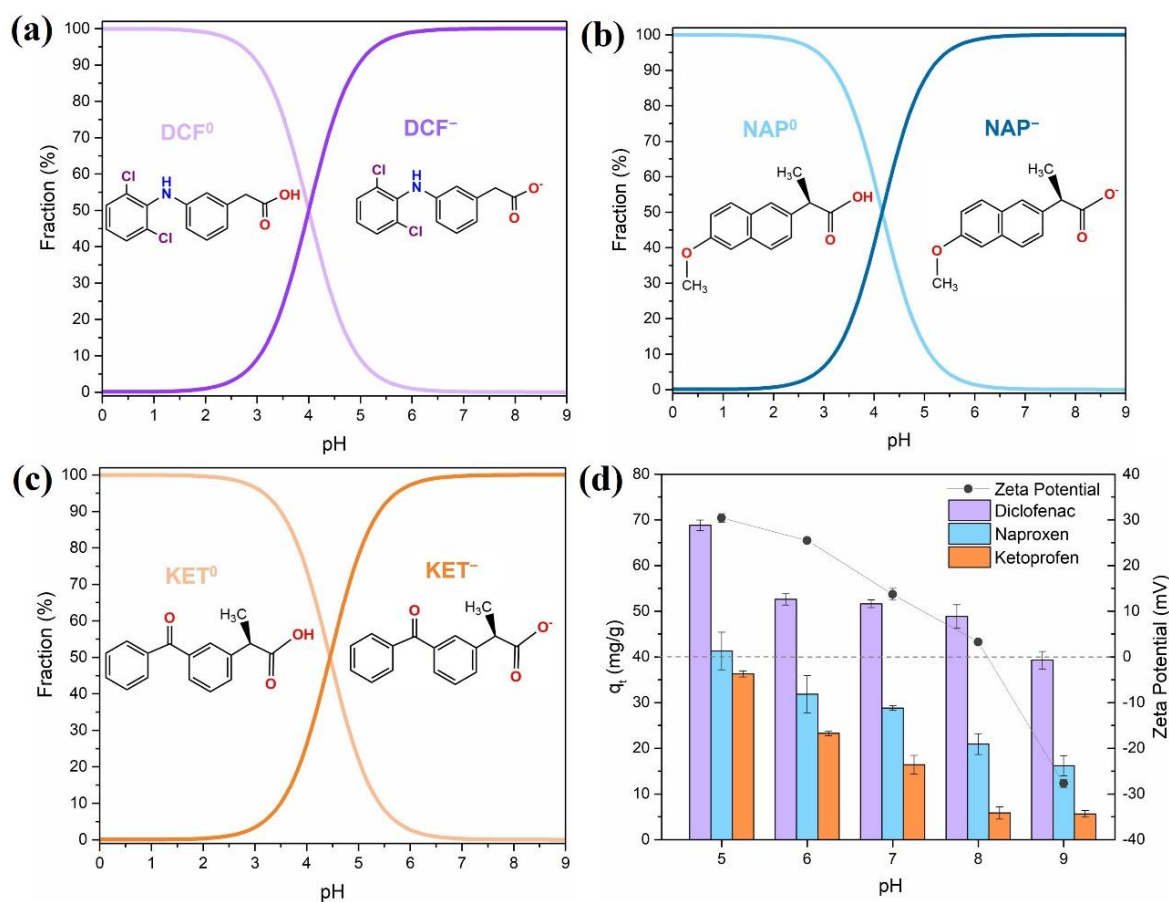
Figure 4. Speciation of (**a**) diclofenac (DCF), (**b**) naproxen (NAP), and (**c**) ketoprofen (KET) as a function of pH in aqueous solution, and (**d**) effect of the pH of the medium (from 5 to 9) on the adsorption of DCF, NAP, and KET (50 mg/L, 5 h contact time, sorbent dose 0.5 mg/mL) using $Fe_3O_4@SiO_2$/TMC/GPTMS particles and zeta potential values of $Fe_3O_4@SiO_2$/TMC/GPTMS particles. Error bars correspond to standard deviations obtained from two replicates.

3.2.2. Influence of Contact Time and Initial NSAIDs Concentration

The influence of contact time on the adsorption of DCF, NAP, and KET at variable initial concentration is shown in Figure 5. The adsorption process was rapid in the first half-hour due to the presence of a high number of available surface sorption sites. The number of existing available sites decreased, and the adsorption sites became saturated for longer contact times. The equilibrium was achieved in 30 min for the lowest concentration tested. To ensure that the equilibrium was reached regardless of the NSAID concentration, the adsorption time was extended up to 5 h. The adsorption capacity increased with the increase of the NSAIDs' initial concentrations.

The affinity of the NSAID compounds towards the magnetic particles was different and followed the trend DCF > NAP > KET. More specifically, the maximum experimental adsorption capacities reached were 100.3 mg/g (0.3153 mmol/g), 78.4 mg/g (0.3108 mmol/g), and 63.7 mg/g (0.2505 mmol/g) for DCF, NAP, and KET, respectively, for an initial concentration of 100 mg/L. The maximum NSAID removal (Figure S3, Supporting Information) was ca. 80%, 60%, and 42% of DCF, NAP, and KET, respectively, for an initial concentration of 10 mg/L. These adsorption experiments were performed at pH = 5, and the surfaces of the particles were positively charged at this pH. As shown in Figure 4a–c, at pH = 5, the NSAID that had a higher fraction of negative species was DCF (90.8% DCF^-, 87.4% NAP^-, and 78.9% KET^-), which promoted the electrostatic interactions and increased the adsorption capacity. Furthermore, as mentioned above, more prominent H-bonding between DCF and particles surface may contribute to increasing adsorption. Blank experiments without magnetic particles were carried out in parallel, and no relevant

losses of DCF, NAP, or KET (<2%) were detected along the time (Figure S4, Supporting Information). This is evidence that the decrease of the NSAIDs concentrations in the presence of the trimethyl chitosan magnetic sorbent was ascribed to adsorption phenomena. Moreover, the removal of the NSAIDs with bare Fe_3O_4 particles (Figure S5, Supporting Information) was minimal (<3%, q_{max} = 2.7 mg/g), which confirms the relevance of the TMC as a surface modifier for the removal of NSAIDs from water.
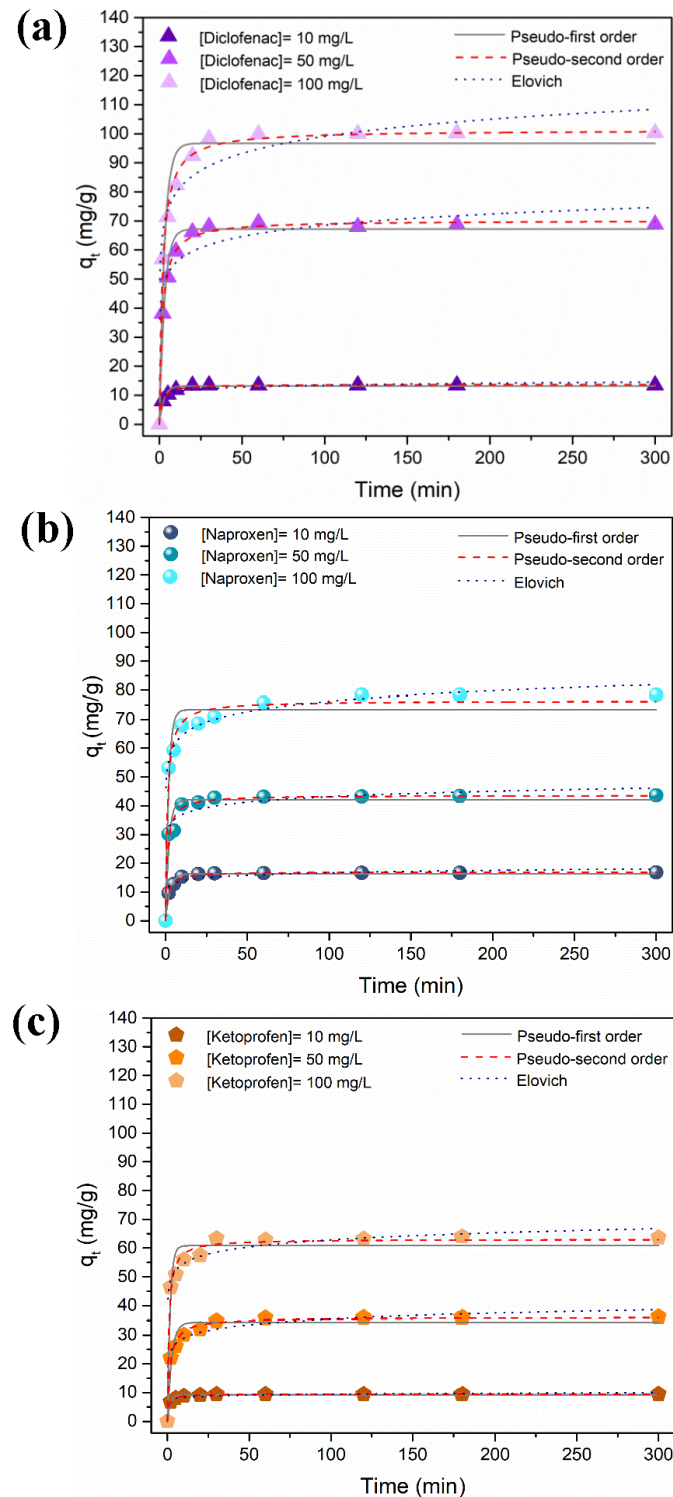

Figure 5. Time profile of adsorption capacity of (**a**) diclofenac, (**b**) naproxen, and (**c**) ketoprofen using the $Fe_3O_4@SiO_2$/TMC/GPTMS particles at variable initial concentrations (10, 50, and 100 mg/L, at pH = 5, contact time of 300 min/5 h) and the corresponding kinetic model fitting.

3.2.3. Kinetic Adsorption Studies

The experimental adsorption data were analyzed using the most common kinetic models to understand the nature of the adsorption process: the pseudo-first-order [63], the pseudo-second-order [64], and the Elovich models [65]. The non-linear forms of the kinetic equations (Equations (S1)–(S3), Supporting Information) were fit to the data. The goodness of fit was determined based on the coefficient of determination (R^2) and the Chi-square test value (χ^2) (Equations (S4) and (S5), Supporting Information). The kinetic parameters and the evaluation of the goodness of fit, obtained by non-linear regression analysis, are reported in Table S2 (Supporting Information), and the kinetic fittings are shown in Figure 5.

Overall, the pseudo-second-order equation provided good fits for all the NSAIDs (R^2 between 0.98 and 0.99 and low χ^2 value), supporting the chemisorption mechanism. Moreover, the values of q_t obtained from the pseudo-second-order model were closer to the experimental results than the qt values predicted from the pseudo-first-order and Elovich models. The pseudo-second-order model assumes that the adsorption rate is reaction-controlled [66]. Thus, these results suggest that the adsorption rate can be governed by the electrostatic interactions between the cationic groups of trimethyl chitosan with the anionic DCF, NAP, and KET molecules [64]. Similar observations have been reported regarding the kinetic profile of NSAID adsorption for other materials [67–69].

3.2.4. Equilibrium Adsorption Studies

The equilibrium adsorption capacity of DCF, NAP, and KET (q_e, mg/g), as a function of the liquid-phase equilibrium concentration of DCF, NAP, and KET (C_e, mg/L), is depicted in Figure 6. In accordance with Giles et al. (1960), isotherms can be divided into four main groups in terms of shape: L, S, H, and C [70]. The isotherm data obtained for all NSAIDs were the L-type (Langmuir), which is characterized by an initial concave region relative to the concentration axis (Figure 6). The equilibrium data were analyzed using the isotherm models of Langmuir [71] and Freundlich [72] (Equations (S6) and (S7), Supporting Information, respectively), which are two-parameter isotherms, and the Sips model [73] (Equation (S8), Supporting Information), which is a three-parameter isotherm. The fitted model parameters are depicted in Table S3 (Supporting Information). Based on the values of R^2 (0.9820–0.9940) and χ^2, it can be concluded that overall, the Sips isotherm provided a good fit of the experimental equilibrium data for DCF, NAP, and KET.

The Langmuir isotherm is one of the most used adsorption isotherm models, and it supposes monolayer coverage of NSAIDs over a homogeneous sorbent surface. The Langmuir monolayer maximum adsorption capacity calculated was 188.5 mg/g (0.5925 mmol/g), 438.1 mg/g (1.7371 mmol/g), and 221.5 mg/g (0.8710 mmol/g) for DCF, NAP, and KET, respectively. The Freundlich isotherm is an empirical model, which assumes the existence of heterogeneous adsorption sites on the surface of the sorbent. Moreover, the Freundlich constant K_F is related to the affinity of the NSAIDs to the $Fe_3O_4@SiO_2$/TMC/GPTMS particles. Thus, a high K_F value for DCF (K_F = 12.5) suggests higher affinity when compared to NAP (K_F = 5.3) and KET (K_F = 4.8). The Sips (or Langmuir–Freundlich) isotherm is a combination of Langmuir and Freundlich isotherms. At low sorbate concentration, the Sips equation reduces to a Freundlich isotherm, while at high sorbate concentrations, it predicts the sorption capacity of a monolayer, characteristic of the Langmuir isotherm [67]. The Sips isotherm equation is characterized by the dimensionless heterogeneity factor (β_S), which varies from 1, in a homogeneous surface, to $\beta_S < 1$, in a heterogeneous surface [74]. For $Fe_3O_4@SiO_2$/TMC/GPTMS particles, the results showed that β_S was smaller than 1 for DCF, NAP, and KET, which indicates heterogeneous surfaces in these sorbents.

For further understanding of the adsorption process, Langmuir isotherm parameters can be used to predict the affinity between the NSAIDs and sorbent particles using a

dimensionless constant called separation factor or equilibrium parameter (R_L), which is expressed by Equation (3) [75] as follows:

$$R_L = \frac{1}{1 + K_L C_0} \tag{3}$$

where K_L (L/mg) is the Langmuir constant, and C_0 (mg/L) is the initial sorbate concentration. The value of R_L shows if the adsorption process is favorable or not as follows: if $R_L = 0$, the adsorption process is irreversible, and this occurs if K_L is very large, indicating very strong adsorption; if $0 < R_L < 1$, the adsorption is favorable, and this is the standard case; $R_L = 1$ indicates that the adsorption isotherm is a straight line, and so it is called linear adsorption; for $R_L > 1$, the adsorption is unfavorable, meaning that desorption happens [67,76]. Figure 6d shows the calculated R_L values versus the initial concentrations of DCF, NAP, and KET. All the R_L values were between 0 and 1, indicating that the adsorption of DCF, NAP, and KET over the $Fe_3O_4@SiO_2$/TMC/GPTMS particles was favorable at the conditions studied. Additionally, lower R_L values at higher initial DCF, NAP, and KET concentrations indicated that adsorption was more favorable at higher sorbate concentrations.
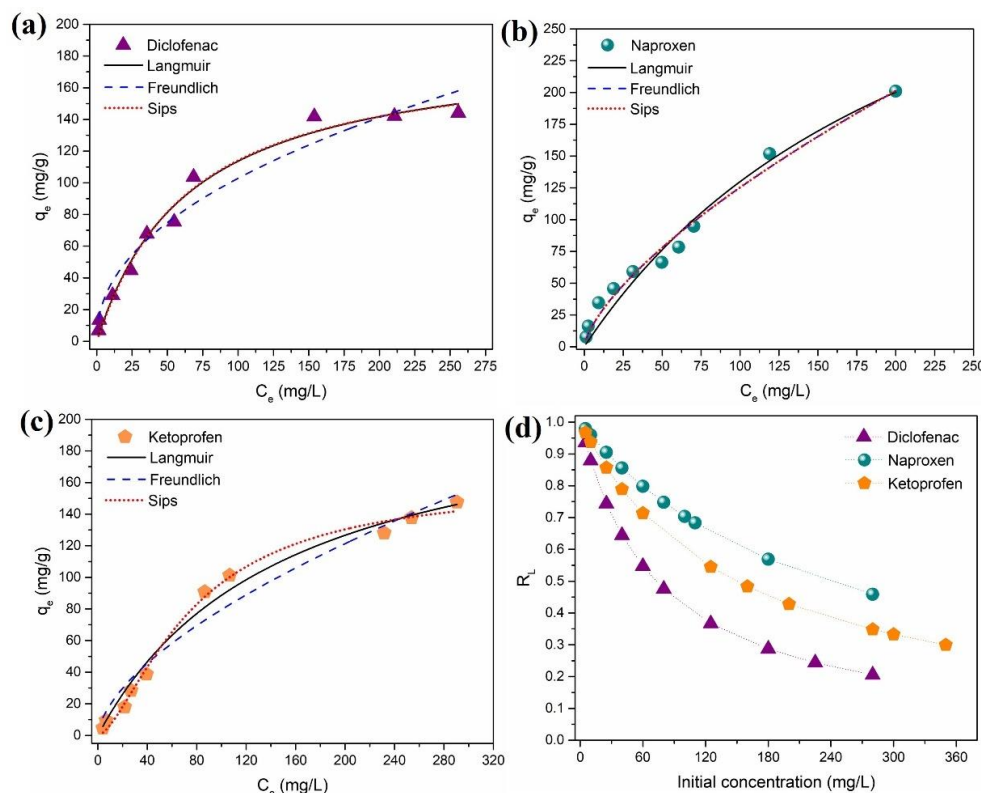

Figure 6. Isotherm data for the adsorption of (**a**) diclofenac, (**b**) naproxen, and (**c**) ketoprofen on the $Fe_3O_4@SiO_2$/TMC/GPTMS particles and model fitting, and (**d**) R_L values for DCF, NAP, and KET as a function of initial concentration sorbate concentration.

3.2.5. Comparison with Other Adsorbents

The efficiency of the proposed particles for the removal of DCF, NAP, and KET was compared with other sorbents reported in the literature. The maximum adsorption capacity of DCF, NAP, and KET was 188.5 mg/g (0.5925 mmol/g), 438.1 mg/g (1.7371 mmol/g), and 221.5 mg/g (0.8710 mmol/g), respectively. As can be seen in Table 2, the particles here developed are very effective in the removal of the selected NSAIDs and present maximum adsorption capacity higher than most of the reported sorbents. In addition, these particles offer the advantage of fast separation and recovery from water using low-energy magnetic

separation. Hence, these results demonstrate the potential of the proposed particles for removing NSAIDs from water.

Table 2. Comparison of the maximum adsorption capacity (q_{max}) of several sorbents reported in the literature for the removal of diclofenac, naproxen, and ketoprofen.

Sorbent	q_{max} (mg/g)	NSAIDs	Equilibrium Time (min)	pH	Reference
$Fe_3O_4@SiO_2$/TMC/GPTMS	188.5 *	Diclofenac	30–60 min	5	This work
	438.1 *	Naproxen			This work
	221.5 *	Ketoprofen			This work
$Fe_3O_4@SiO_2$/SiHTCC	240.4 *	Diclofenac	30–300 min	6	[20]
Chitosan-modified waste tire crumb rubber	17.0	Diclofenac	120 min	6	[69]
	2.3	Naproxen			
Green copper nanoadsorbent	33.9 *	Diclofenac	60 min	4.5	[77]
	36.0 *	Naproxen			
Activated biochar	372 *	Diclofenac	n.a	7	[78]
	290 *	Naproxen			
Poly(4-vinylpyridine)-functionalized magnetic Al-MOF	31.6 *	Naproxen	120 min	4.7	[79]
Silica-magnetic/graphene oxide	31.1	Naproxen	60 min	5	[80]
Carbon-based magnetic adsorbent	87.7 *	Naproxen	150 min	5	[81]
Activated carbon from apricot waste	106.3 *	Naproxen	20 min	5.8	[82]
Biopolymer electrospun nanofibers	125.0 *	Diclofenac	30 min	5.5	[83]
	111.1 *	Ketoprofen			
Nitrogen-doped reduced graphene oxide/Fe_3O_4	468 *	Ketoprofen	360 min	6.8	[84]
Carbon nanotubes	207.6 *	Ketoprofen	5–10 min	n.a	[85]
$NiFe_2O_4$/activated carbon	97.7 **	Ketoprofen	240 min	2	[86]

* Maximum Langmuir adsorption capacity; ** maximum Sips adsorption capacity; n.a: not available; HTCC: N-(2-hydroxypropyl)-3-trimethylammonium chitosan chloride; MOF: metal organic framework.

4. Conclusions

We have reported here studies on batch mode for the adsorption of three selected NSAIDs frequently detected in aquatic media, using new magnetic nanosorbents based on trimethyl chitosan. The resulting nanosorbents removed diclofenac, naproxen, and ketoprofen efficiently from aqueous solutions, denoting high adsorption capacity. This improved efficiency is related to the high affinity of functional groups from trimethyl chitosan, used here as a surface modifier, to NSAIDs molecules, along with reduced particle dimensions and high surface-to-volume ratios. It was observed that the affinity of the NSAID compounds towards the magnetic particles followed the trend DCF > NAP > KET. Therefore, this magnetic biosorbent based on quaternary chitosan offers new possibilities for water purification contaminated with diclofenac, naproxen, and ketoprofen by applying magnetic-assisted cleaning technologies. Future perspectives for integrating these new nanosorbents in adsorption technologies are promising due to their effectiveness as compared to other materials described in the literature.

Supplementary Materials: The following are available online at https://www.mdpi.com/article/10.3390/coatings11080964/s1, Figure S1: Calibration curves for diclofenac (0.12–12.0 mg/L), naproxen (0.12–3 mg/L), and ketoprofen (0.12–12.0 mg/L) in ultra-pure water, providing a linear relation between the absorbance and the concentration, Figure S2: SEM images of (a) SiO_2/TMC/GPTMS and (c) SiO_2 particles and ATR-FTIR spectra of (b) SiO_2/TMC/GPTMS and (d) SiO_2 particles, Figure S3: Time profile of removal percentage of NSAIDs at variable (a) DCF, (b) NAP, and (c) KET initial concentration (10, 50, and 100 mg/L), using the particles $Fe_3O_4@SiO_2$/TMC/GPTMS, for 5 h (300 min), Figure S4: Variation of diclofenac, naproxen, and ketoprofen concentration on

control experiments performed in absence of adsorbent particles to assess the loss of DCF, NAP, and KET caused by other phenomena than adsorption on sorbents, Figure S5: Time profile of removal percentage and (b) adsorption capacity of diclofenac, naproxen, and ketoprofen at 50 mg/L, using Fe_3O_4 particles, for 5 h (300 min), Figure S6: Kinetic parameters estimated from pseudo-first and -second order and Elovich models, and evaluation of their fittings for diclofenac, naproxen, and ketoprofen, using $Fe_3O_4@SiO_2$/TMC/GPTMS particles, Table S1: Selected characteristics and structures of NSAIDs, Table S2: ^{13}C CP/MAS, ^{29}Si MAS, and ^{29}Si CP/MAS NMR chemical shifts for TMC, SiO_2/TMC/GPTMS, and SiO_2 particles and quantification of the ^{29}Si Q^n resonances, Table S3: Equilibrium model parameters obtained from model fitting to experimental sorption data of $Fe_3O_4@SiO_2$/TMC/GPTMS for the removal of DCF, NAP, and KET, together with the goodness of fit.

Author Contributions: Conceptualization, S.F.S. and A.L.D.-d.-S.; methodology, S.F.S. and A.L.D.-d.-S.; validation, T.T. and A.L.D.-d.-S.; formal analysis, S.F.S. and A.L.D.-d.-S.; investigation, S.F.S. and A.L.D.-d.-S.; resources, T.T. and A.L.D.-d.-S.; data curation, S.F.S. and A.L.D.-d.-S.; writing—original draft preparation, S.F.S.; writing—review and editing, T.T. and A.L.D.-d.-S.; supervision, T.T. and A.L.D.-d.-S.; funding acquisition, T.T. and A.L.D.-d.-S. All authors have read and agreed to the published version of the manuscript.

Institutional Review Board Statement: Not applicable.

Informed Consent Statement: Not applicable.

Data Availability Statement: All data reported in this paper is contained within the manuscript and supplementary material.

Conflicts of Interest: The authors declare no conflict of interest.

References

1. Golovko, O.; Örn, S.; Sörengård, M.; Frieberg, K.; Nassazzi, W.; Lai, F.Y.; Ahrens, L. Occurrence and removal of chemicals of emerging concern in wastewater treatment plants and their impact on receiving water systems. *Sci. Total Environ.* **2021**, *754*, 142122. [CrossRef]
2. Tran, N.H.; Reinhard, M.; Gin, K.Y.-H. Occurrence and fate of emerging contaminants in municipal wastewater treatment plants from different geographical regions-a review. *Water Res.* **2018**, *133*, 182–207. [CrossRef]
3. Fent, K.; Weston, A.; Caminada, D. Ecotoxicology of human pharmaceuticals. *Aquat. Toxicol.* **2006**, *76*, 122–159. [CrossRef]
4. Sousa, J.C.G.; Ribeiro, A.R.; Barbosa, M.O.; Pereira, M.F.R.; Silva, A.M.T. A review on environmental monitoring of water organic pollutants identified by EU guidelines. *J. Hazard. Mater.* **2018**, *344*, 146–162. [CrossRef] [PubMed]
5. Barbosa, M.O.; Moreira, N.F.F.; Ribeiro, A.R.; Pereira, M.F.R.; Silva, A.M.T. Occurrence and removal of organic micropollutants: An overview of the watch list of EU Decision 2015/495. *Water Res.* **2016**, *94*, 257–279. [CrossRef]
6. Izadi, P.; Izadi, P.; Salem, R.; Papry, S.A.; Magdouli, S.; Pulicharla, R.; Brar, S.K. Non-steroidal anti-inflammatory drugs in the environment: Where were we and how far we have come? *Environ. Pollut.* **2020**, *267*, 115370. [CrossRef] [PubMed]
7. Mlunguza, N.Y.; Ncube, S.; Nokwethemba Mahlambi, P.; Chimuka, L.; Madikizela, L.M. Adsorbents and removal strategies of non-steroidal anti-inflammatory drugs from contaminated water bodies. *J. Environ. Chem. Eng.* **2019**, *7*, 103142. [CrossRef]
8. Kermia, A.E.B.; Fouial-Djebbar, D.; Trari, M. Occurrence, fate and removal efficiencies of pharmaceuticals in wastewater treatment plants (WWTPs) discharging in the coastal environment of Algiers. *Comptes Rendus Chim.* **2016**, *19*, 963–970. [CrossRef]
9. Couto, C.F.; Lange, L.C.; Amaral, M.C.S. Occurrence, fate and removal of pharmaceutically active compounds (PhACs) in water and wastewater treatment plants—A review. *J. Water Process Eng.* **2019**, *32*, 100927. [CrossRef]
10. Luo, Y.; Guo, W.; Ngo, H.H.; Nghiem, L.D.; Hai, F.I.; Zhang, J.; Liang, S.; Wang, X.C. A review on the occurrence of micropollutants in the aquatic environment and their fate and removal during wastewater treatment. *Sci. Total Environ.* **2014**, *473–474*, 619–641. [CrossRef] [PubMed]
11. Petrie, B.; Camacho-Muñoz, D. Analysis, fate and toxicity of chiral non-steroidal anti-inflammatory drugs in wastewaters and the environment: A review. *Environ. Chem. Lett.* **2021**, *19*, 43–75.

12. Hena, S.; Gutierrez, L.; Croué, J.-P. Removal of pharmaceutical and personal care products (PPCPs) from wastewater using microalgae: A review. *J. Hazard. Mater.* **2021**, *403*, 124041. [CrossRef] [PubMed]

13. Gros, M.; Petrović, M.; Ginebreda, A.; Barceló, D. Removal of pharmaceuticals during wastewater treatment and environmental risk assessment using hazard indexes. *Environ. Int.* **2010**, *36*, 15–26. [CrossRef]

14. Zaied, B.K.; Rashid, M.; Nasrullah, M.; Zularisam, A.W.; Pant, D.; Singh, L. A comprehensive review on contaminants removal from pharmaceutical wastewater by electrocoagulation process. *Sci. Total Environ.* **2020**, *726*, 138095. [CrossRef]

15. Zupanc, M.; Kosjek, T.; Petkovšek, M.; Dular, M.; Kompare, B.; Širok, B.; Blažeka, Ž.; Heath, E. Removal of pharmaceuticals from wastewater by biological processes, hydrodynamic cavitation and UV treatment. *Ultrason. Sonochem.* **2013**, *20*, 1104–1112. [CrossRef]

16. Soares, S.F.; Fernandes, T.; Trindade, T.; Daniel-da-Silva, A.L. Surface engineered magnetic biosorbents for water treatment. In *Green Adsorbents for Pollutant Removal. Environmental Chemistry for a Sustainable World*; Crini, G., Lichtfouse, E., Eds.; Springer: Cham, Switzerland, 2018; pp. 301–342. ISBN 978-3-319-92111-2.

17. Budnyak, T.M.; Yanovska, E.S.; Kołodyńska, D.; Sternik, D.; Pylypchuk, I.V.; Ischenko, M.V.; Tertykh, V.A. Preparation and properties of organomineral adsorbent obtained by sol–gel technology. *J. Therm. Anal. Calorim.* **2016**, *125*, 1335–1351. [CrossRef]

18. Salama, A. Polysaccharides/silica hybrid materials: New perspectives for sustainable raw materials. *J. Carbohydr. Chem.* **2016**, *35*, 131–149. [CrossRef]

19. Soares, S.F.; Rocha, M.J.; Ferro, M.; Amorim, C.O.; Amaral, J.S.; Trindade, T.; Daniel-da-Silva, A.L. Magnetic nanosorbents with siliceous hybrid shells of alginic acid and carrageenan for removal of ciprofloxacin. *Int. J. Biol. Macromol.* **2019**, *139*, 827–841. [CrossRef]

20. Soares, S.F.; Fernandes, T.; Sacramento, M.; Trindade, T.; Daniel-da-Silva, A.L. Magnetic quaternary chitosan hybrid nanoparticles for the efficient uptake of diclofenac from water. *Carbohydr. Polym.* **2019**, *203*, 35–44. [CrossRef] [PubMed]

21. Ogoshi, T.; Chujo, Y. Organic–inorganic polymer hybrids prepared by the sol-gel method. *Compos. Interfaces* **2005**, *11*, 539–566. [CrossRef]

22. Wang, D.; Liu, W.; Feng, Q.; Dong, C.; Liu, Q.; Duan, L.; Huang, J.; Zhu, W.; Li, Z.; Xiong, J.; et al. Effect of inorganic/organic ratio and chemical coupling on the performance of porous silica/chitosan hybrid scaffolds. *Mater. Sci. Eng. C* **2017**, *70*, 969–975. [CrossRef] [PubMed]

23. Wang, D.; Romer, F.; Connell, L.; Walter, C.; Saiz, E.; Yue, S.; Lee, P.D.; McPhail, D.S.; Hanna, J.V.; Jones, J.R. Highly flexible silica/chitosan hybrid scaffolds with oriented pores for tissue regeneration. *J. Mater. Chem. B* **2015**, *3*, 7560–7576. [CrossRef]

24. Connell, L.S.; Romer, F.; Suárez, M.; Valliant, E.M.; Zhang, Z.; Lee, P.D.; Smith, M.E.; Hanna, J.V.; Jones, J.R. Chemical characterisation and fabrication of chitosan–silica hybrid scaffolds with 3-glycidoxypropyl trimethoxysilane. *J. Mater. Chem. B* **2014**, *2*, 668–680. [CrossRef]

25. Mallakpour, S.; Madani, M. A review of current coupling agents for modification of metal oxide nanoparticles. *Prog. Org. Coat.* **2015**, *86*, 194–207. [CrossRef]

26. Roosen, J.; Spooren, J.; Binnemans, K. Adsorption performance of functionalized chitosan–silica hybrid materials toward rare earths. *J. Mater. Chem. A* **2014**, *2*, 19415–19426. [CrossRef]

27. Bakshi, P.S.; Selvakumar, D.; Kadirvelu, K.; Kumar, N.S. Chitosan as an environment friendly biomaterial–A review on recent modifications and applications. *Int. J. Biol. Macromol.* **2020**, *150*, 1072–1083. [CrossRef] [PubMed]

28. Kyzas, G.; Bikiaris, D. Recent modifications of chitosan for adsorption applications: A critical and systematic review. *Mar. Drugs* **2015**, *13*, 312–337. [CrossRef]

29. Negm, N.A.; Hefni, H.H.H.; Abd-Elaal, A.A.A.; Badr, E.A.; Abou Kana, M.T.H. Advancement on modification of chitosan biopolymer and its potential applications. *Int. J. Biol. Macromol.* **2020**, *152*, 681–702. [CrossRef]

30. Wu, M.; Long, Z.; Xiao, H.; Dong, C. Recent research progress on preparation and application of *N,N,N*-trimethyl chitosan. *Carbohydr. Res.* **2016**, *434*, 27–32. [CrossRef]

31. Pinheiro, P.C.; Daniel-da-Silva, A.L.; Nogueira, H.I.S.; Trindade, T. Functionalized inorganic nanoparticles for magnetic separation and SERS detection of water pollutants. *Eur. J. Inorg. Chem.* **2018**, *2018*, 3443–3461. [CrossRef]

32. Chibowski, E.; Szcześ, A. Magnetic water treatment–A review of the latest approaches. *Chemosphere* **2018**, *203*, 54–67. [CrossRef]

33. Soares, S.F.; Fernandes, T.; Trindade, T.; Daniel-da-Silva, A.L. Trimethyl chitosan/siloxane-hybrid coated Fe_3O_4 nanoparticles for the uptake of sulfamethoxazole from water. *Molecules* **2019**, *24*, 1958. [CrossRef]

34. Oliveira-Silva, R.; Pinto da Costa, J.; Vitorino, R.; Daniel-da-Silva, A.L. Magnetic chelating nanoprobes for enrichment and selective recovery of metalloproteases from human saliva. *J. Mater. Chem. B* **2015**, *3*, 238–249. [CrossRef]

35. Soares, S.F.; Trindade, T.; Daniel-da-Silva, A.L. Carrageenan-silica hybrid nanoparticles prepared by a non-emulsion method. *Eur. J. Inorg. Chem.* **2015**, *2015*, 4588–4594. [CrossRef]

36. Green, D.; Lin, J.; Lam, Y.-F.; Hu, M.Z.-C.; Schaefer, D.W.; Harris, M. Size, volume fraction, and nucleation of Stober silica nanoparticles. *J. Colloid Interface Sci.* **2003**, *266*, 346–358. [CrossRef]

37. Joint Committee for Powder Diffraction Studies, JCPDS, card no. 19-0629.

38. Biswas, R.K.; Khan, P.; Mukherjee, S.; Mukhopadhyay, A.K.; Ghosh, J.; Muraleedharan, K. Study of short range structure of amorphous Silica from PDF using Ag radiation in laboratory XRD system, RAMAN and NEXAFS. *J. Non. Cryst. Solids* **2018**, *488*, 1–9. [CrossRef]

39. Namduri, H.; Nasrazadani, S. Quantitative analysis of iron oxides using Fourier transform infrared spectrophotometry. *Corros. Sci.* **2008**, *50*, 2493–2497. [CrossRef]

40. Mansur, H.S.; Mansur, A.A.P.; Curti, E.; De Almeida, M.V. Functionalized-chitosan/quantum dot nano-hybrids for nanomedicine applications: Towards biolabeling and biosorbing phosphate metabolites. *J. Mater. Chem. B* **2013**, *1*, 1696. [CrossRef] [PubMed]

41. de Britto, D.; Assis, O.B.G. A novel method for obtaining a quaternary salt of chitosan. *Carbohydr. Polym.* **2007**, *69*, 305–310. [CrossRef]

42. Schramm, C. High temperature ATR-FTIR characterization of the interaction of polycarboxylic acids and organotrialkoxysilanes with cellulosic material. *Spectrochim. Acta Part A Mol. Biomol. Spectrosc.* **2020**, *243*, 118815. [CrossRef]

43. Ma, J.; Duan, L.; Lu, J.; Lyu, B.; Gao, D.; Wu, X. Fabrication of modified hydrogenated castor oil/GPTMS-ZnO composites and effect on UV resistance of leather. *Sci. Rep.* **2017**, *7*, 3742. [CrossRef]

44. Šapić, I.M.; Bistričić, L.; Volovšek, V.; Dananić, V.; Furić, K. DFT study of molecular structure and vibrations of 3-glycidoxypropyltrimethoxysilane. *Spectrochim. Acta Part A Mol. Biomol. Spectrosc.* **2009**, *72*, 833–840. [CrossRef]

45. Dun, Y.; Zuo, Y. Preparation and characterization of a GPTMS/graphene coating on AA-2024 alloy. *Appl. Surf. Sci.* **2017**, *416*, 492–502. [CrossRef]

46. Balgude, D.; Konge, K.; Sabnis, A. Synthesis and characterization of sol–gel derived CNSL based hybrid anti-corrosive coatings. *J. Sol-Gel Sci. Technol.* **2014**, *69*, 155–165. [CrossRef]

47. Zhang, C.; Zhang, C.; Sun, J.; Ding, R.; Zhang, Q.; Xu, Y. A double-layer moisture barrier & antireflective film based on bridged polysilsesquioxane and porous silica. *RSC Adv.* **2015**, *5*, 56998–57005.

48. Tiringer, U.; Milošev, I.; Durán, A.; Castro, Y. Hybrid sol–gel coatings based on GPTMS/TEOS containing colloidal SiO$_2$ and cerium nitrate for increasing corrosion protection of aluminium alloy 7075-T6. *J. Sol-Gel Sci. Technol.* **2018**, *85*, 546–557. [CrossRef]

49. de Britto, D.; Forato, L.A.; Assis, O.B.G. Determination of the average degree of quaternization of *N,N,N*-trimethylchitosan by solid state ^{13}C NMR. *Carbohydr. Polym.* **2008**, *74*, 86–91. [CrossRef]

50. de Britto, D.; Celi Goy, R.; Campana Filho, S.P.; Assis, O.B.G. Quaternary salts of chitosan: History, antimicrobial features, and prospects. *Int. J. Carbohydr. Chem.* **2011**, *2011*, 1–12. [CrossRef]

51. Liu, B.; Li, X.; Zheng, C.; Wang, X.; Sun, R. Facile and green synthesis of silver nanoparticles in quaternized carboxymethyl chitosan solution. *Nanotechnology* **2013**, *24*, 235601. [CrossRef]

52. Gouveia, Z.; Perinpanayagam, H.; Zhu, J. Development of robust chitosan–silica class II hybrid coatings with antimicrobial properties for titanium implants. *Coatings* **2020**, *10*, 534. [CrossRef]

53. Vueva, Y.; Connell, L.S.; Chayanun, S.; Wang, D.; McPhail, D.S.; Romer, F.; Hanna, J.V.; Jones, J.R. Silica/alginate hybrid biomaterials and assessment of their covalent coupling. *Appl. Mater. Today* **2018**, *11*, 1–12. [CrossRef]

54. Babonneau, F.; Baccile, N.; Laurent, G.; Maquet, J.; Azaïs, T.; Gervais, C.; Bonhomme, C. Solid-state nuclear magnetic resonance: A valuable tool to explore organic-inorganic interfaces in silica-based hybrid materials. *Comptes Rendus Chim.* **2010**, *13*, 58–68. [CrossRef]

55. Lippach, A.K.W.; Krämer, R.; Hansen, M.R.; Roos, S.; Stöwe, K.; Stommel, M.; Wenz, G.; Maier, W.F. Synthesis and mechanical properties of organic-inorganic hybrid materials from lignin and polysiloxanes. *ChemSusChem* **2012**, *5*, 1778–1786. [CrossRef]

56. Wang, T.; Liu, S.; Gao, G.; Zhao, P.; Lu, N.; Lun, X.; Hou, X. Magnetic solid phase extraction of non-steroidal anti-inflammatory drugs from water samples using a metal organic framework of type Fe$_3$O$_4$/MIL-101(Cr), and their quantitation by UPLC-MS/MS. *Microchim. Acta* **2017**, *184*, 2981–2990. [CrossRef]

57. Mao, N.; Huang, L.; Shuai, Q. Facile synthesis of porous carbon for the removal of diclofenac sodium from water. *ACS Omega* **2019**, *4*, 15051–15060. [CrossRef]

58. Rasheed, T.; Bilal, M.; Hassan, A.A.; Nabeel, F.; Bharagava, R.N.; Romanholo Ferreira, L.F.; Tran, H.N.; Iqbal, H.M.N. Environmental threatening concern and efficient removal of pharmaceutically active compounds using metal-organic frameworks as adsorbents. *Environ. Res.* **2020**, *185*, 109436. [CrossRef]

59. Pap, S.; Taggart, M.A.; Shearer, L.; Li, Y.; Radovic, S.; Turk Sekulic, M. Removal behaviour of NSAIDs from wastewater using a P-functionalised microporous carbon. *Chemosphere* **2021**, *264*, 128439. [CrossRef]

60. Mohiuddin, I.; Grover, A.; Aulakh, J.S.; Malik, A.K.; Lee, S.S.; Brown, R.J.C.; Kim, K.-H. Starch-Mg/Al layered double hydroxide composites as an efficient solid phase extraction sorbent for non-steroidal anti-inflammatory drugs as environmental pollutants. *J. Hazard. Mater.* **2021**, *401*, 123782. [CrossRef]

61. Maryam, B.; Buscio, V.; Odabasi, S.U.; Buyukgungor, H. A study on behavior, interaction and rejection of paracetamol, diclofenac and ibuprofen (PhACs) from wastewater by nanofiltration membranes. *Environ. Technol. Innov.* **2020**, *18*, 100641. [CrossRef]

62. Seo, P.W.; Bhadra, B.N.; Ahmed, I.; Khan, N.A.; Jhung, S.H. Adsorptive removal of pharmaceuticals and personal care products from water with functionalized metal-organic frameworks: Remarkable adsorbents with hydrogen-bonding abilities. *Sci. Rep.* **2016**, *6*, 34462. [CrossRef]

63. Lagergren, S. *Zur Theorie der Sogenannten Adsorption Gelöster Stoffe*; Handlingar, Ed.; Springer: Berlin, Germany, 1907; Volume 2, ISBN 0368-6590.

64. Ho, Y.S.; McKay, G. Pseudo-second order model for sorption processes. *Process Biochem.* **1999**, *34*, 451–465. [CrossRef]

65. Chien, S.H.; Clayton, W.R. Application of Elovich equation to the kinetics of phosphate release and sorption in soils. *Soil Sci. Soc. Am. J.* **1980**, *44*, 265. [CrossRef]

66. Xiao, Y.; Azaiez, J.; Hill, J.M. Erroneous application of pseudo-second-order adsorption kinetics model: Ignored assumptions and spurious correlations. *Ind. Eng. Chem. Res.* **2018**, *57*, 2705–2709. [CrossRef]

67. Hasan, Z.; Choi, E.-J.; Jhung, S.H. Adsorption of naproxen and clofibric acid over a metal–organic framework MIL-101 functionalized with acidic and basic groups. *Chem. Eng. J.* **2013**, *219*, 537–544. [CrossRef]

68. Hasan, Z.; Jeon, J.; Jhung, S.H. Adsorptive removal of naproxen and clofibric acid from water using metal-organic frameworks. *J. Hazard. Mater.* **2012**, *209–210*, 151–157. [CrossRef] [PubMed]

69. Phasuphan, W.; Praphairaksit, N.; Imyim, A. Removal of ibuprofen, diclofenac, and naproxen from water using chitosan-modified waste tire crumb rubber. *J. Mol. Liq.* **2019**, *294*, 111554. [CrossRef]

70. Giles, C.H.; MacEwan, T.H.; Nakhwa, S.N.; Smith, D. 786. Studies in adsorption. Part XI. A system of classification of solution adsorption isotherms, and its use in diagnosis of adsorption mechanisms and in measurement of specific surface areas of solids. *J. Chem. Soc.* **1960**, *14*, 3973–3993. [CrossRef]

71. Langmuir, I. The adsorption of gases on plane surfaces of glass, mica and platinum. *J. Am. Chem. Soc.* **1918**, *40*, 1361–1403. [CrossRef]

72. Freundlich, H.Z. Concerning adsorption in solutions. *Zeitschrift für Phys. Chem.* **1906**, *57*, 444–448.

73. Sips, R. On the structure of a catalyst surface. *J. Chem. Phys.* **1948**, *16*, 490. [CrossRef]

74. Ramadoss, R.; Subramaniam, D. Removal of divalent nickel from aqueous solution using blue-green marine algae: Adsorption modeling and applicability of various isotherm models. *Sep. Sci. Technol.* **2019**, *54*, 943–961. [CrossRef]

75. Weber, T.W.; Chakravorti, R.K. Pore and solid diffusion models for fixed-bed adsorbers. *AIChE J.* **1974**, *20*, 228–238. [CrossRef]

76. Liu, H.; Dong, Y.; Wang, H.; Liu, Y. Adsorption behavior of ammonium by a bioadsorbent–Boston ivy leaf powder. *J. Environ. Sci.* **2010**, *22*, 1513–1518. [CrossRef]

77. Husein, D.Z.; Hassanien, R.; Al-Hakkani, M.F. Green-synthesized copper nano-adsorbent for the removal of pharmaceutical pollutants from real wastewater samples. *Heliyon* **2019**, *5*, e02339. [CrossRef] [PubMed]

78. Jung, C.; Boateng, L.K.; Flora, J.R.V.; Oh, J.; Braswell, M.C.; Son, A.; Yoon, Y. Competitive adsorption of selected non-steroidal anti-inflammatory drugs on activated biochars: Experimental and molecular modeling study. *Chem. Eng. J.* **2015**, *264*, 1–9. [CrossRef]

79. Li, Y.; Wang, Y.; He, L.; Meng, L.; Lu, H.; Li, X. Preparation of poly(4-vinylpyridine)-functionalized magnetic Al-MOF for the removal of naproxen from aqueous solution. *J. Hazard. Mater.* **2020**, *383*, 121144. [CrossRef]

80. Mohammadi Nodeh, M.K.; Radfard, M.; Zardari, L.A.; Rashidi Nodeh, H. Enhanced removal of naproxen from wastewater using silica magnetic nanoparticles decorated onto graphene oxide; parametric and equilibrium study. *Sep. Sci. Technol.* **2018**, *53*, 2476–2485. [CrossRef]

81. İlbay, Z.; Şahin, S.; Kerkez, Ö.; Bayazit, Ş.S. Isolation of naproxen from wastewater using carbon-based magnetic adsorbents. *Int. J. Environ. Sci. Technol.* **2015**, *12*, 3541–3550. [CrossRef]

82. Önal, Y.; Akmil-Başar, C.; Sarıcı-Özdemir, Ç. Elucidation of the naproxen sodium adsorption onto activated carbon prepared from waste apricot: Kinetic, equilibrium and thermodynamic characterization. *J. Hazard. Mater.* **2007**, *148*, 727–734. [CrossRef] [PubMed]

83. Kebede, T.G.; Dube, S.; Nindi, M.M. Biopolymer electrospun nanofibres for the adsorption of pharmaceuticals from water systems. *J. Environ. Chem. Eng.* **2019**, *7*, 103330. [CrossRef]

84. Peng, G.; Zhang, M.; Deng, S.; Shan, D.; He, Q.; Yu, G. Adsorption and catalytic oxidation of pharmaceuticals by nitrogen-doped reduced graphene oxide/Fe_3O_4 nanocomposite. *Chem. Eng. J.* **2018**, *341*, 361–370. [CrossRef]

85. Lawal, I.A.; Lawal, M.M.; Akpotu, S.O.; Azeez, M.A.; Ndungu, P.; Moodley, B. Theoretical and experimental adsorption studies of sulfamethoxazole and ketoprofen on synthesized ionic liquids modified CNTs. *Ecotoxicol. Environ. Saf.* **2018**, *161*, 542–552. [CrossRef] [PubMed]

86. Fröhlich, A.C.; Foletto, E.L.; Dotto, G.L. Preparation and characterization of $NiFe_2O_4$/activated carbon composite as potential magnetic adsorbent for removal of ibuprofen and ketoprofen pharmaceuticals from aqueous solutions. *J. Clean. Prod.* **2019**, *229*, 828–837. [CrossRef]